



HAL
open science

Descanned Fast Light Targeting (deFLiT) Two-Photon Optogenetics

Cécile Telliez, Vincent de Sars, Valentina Emiliani, Emiliano Ronzitti

► **To cite this version:**

Cécile Telliez, Vincent de Sars, Valentina Emiliani, Emiliano Ronzitti. Descanned Fast Light Targeting (deFLiT) Two-Photon Optogenetics. Biomedical optics express, In press. hal-04250044

HAL Id: hal-04250044

<https://hal.science/hal-04250044>

Submitted on 19 Oct 2023

HAL is a multi-disciplinary open access archive for the deposit and dissemination of scientific research documents, whether they are published or not. The documents may come from teaching and research institutions in France or abroad, or from public or private research centers.

L'archive ouverte pluridisciplinaire **HAL**, est destinée au dépôt et à la diffusion de documents scientifiques de niveau recherche, publiés ou non, émanant des établissements d'enseignement et de recherche français ou étrangers, des laboratoires publics ou privés.

Descanned Fast Light Targeting (deFLiT) Two-Photon Optogenetics

CECILE TELLIEZ¹, VINCENT DE SARS¹, VALENTINA EMILIANI^{1,2} AND EMILIANO RONZITTI^{1,3}

¹ Sorbonne Université, INSERM, CNRS, Institut de la Vision, 75012 Paris

² valentina.emiliani@inserm.fr

³ emiliano.ronzitti@inserm.fr

Abstract: Two-photon light-targeting optogenetics allows controlling selected subsets of neurons with near single-cell resolution and high temporal precision. To push forward this approach, we recently proposed a fast light-targeting approach (FLiT) to rapidly scan multiple holograms tiled on a spatial light modulator (SLM). This allowed generating sub-ms timely-controlled switch of light patterns enabling to reduce the power budget for multi-target excitation and increase the temporal precision for relative spike tuning in a circuit. Here, we modified the optical design of FLiT by including a de-scan unit (deFLiT) to keep the holographic illumination centered at the middle of the objective pupil independently of the position of the tiled hologram on the SLM. This enables enlarging the number of usable holograms and reaching extended on-axis excitation volumes, and therefore increasing even further the power gain and temporal precision of conventional FLiT.

© 2022 Optica Publishing Group under the terms of the [Optica Publishing Group Open Access Publishing Agreement](#)

References

1. O. Yizhar, L. E. Fenno, T. J. Davidson, M. Mogri, and K. Deisseroth, "Optogenetics in neural systems.," *Neuron* **71**(1), 9–34 (2011).
2. L. Fenno, O. Yizhar, and K. Deisseroth, "The Development and Application of Optogenetics," *Annu. Rev. Neurosci.* **34**(1), 389–412 (2011).
3. F. Schneider, C. Grimm, and P. Hegemann, "Biophysics of Channelrhodopsin.," *Annu. Rev. Biophys.* **44**, 167–86 (2015).
4. E. Ronzitti, C. Ventalon, M. Canepari, B. C. Forget, E. Papagiakoumou, and V. Emiliani, "Recent advances in patterned photostimulation for optogenetics," *J. Opt.* (2017).
5. E. Ronzitti, V. Emiliani, and E. Papagiakoumou, "Methods for Three-Dimensional All-Optical Manipulation of Neural Circuits," *Front.Cell.Neurosci.* **12**, 469 (2018).
6. A. M. Packer, B. Roska, and M. Häusser, "Targeting neurons and photons for optogenetics.," *Nat. Neurosci.* **16**(7), 805–15 (2013).
7. H. Adesnik and L. Abdeladim, "Probing neural codes with two-photon holographic optogenetics," *Nat. Neurosci.* **24**(10), 1356–1366 (2021).
8. A. M. Packer, D. S. Peterka, J. J. Hirtz, R. Prakash, K. Deisseroth, R. Yuste, O. Yizhar, B. Grewe, C. Ramakrishnan, N. Wang, I. Goshen, A. M. Packer, D. S. Peterka, R. Yuste, M. J. Schnitzer, and K. Deisseroth, "Two-photon optogenetics of dendritic spines and neural circuits.," *Nat. Methods* **9**(12), 1202–5 (2012).
9. J. P. Rickgauer, K. Deisseroth, and D. W. Tank, "Simultaneous cellular-resolution optical perturbation and imaging of place cell firing fields," *Nat. Neurosci.* **17**(12), 1816–24 (2014).
10. E. Papagiakoumou, F. Anselmi, A. Bègue, V. de Sars, J. Glückstad, E. Y. Isacoff, and V. Emiliani, "Scanless two-photon excitation of channelrhodopsin-2.," *Nat. Methods* **7**(10), 848–54 (2010).
11. A. R. Mardinly, I. A. Oldenburg, N. C. Pégard, S. Sridharan, E. H. Lyall, K. Chesnov, S. G. Brohawn, L. Waller, and H. Adesnik, "Precise multimodal optical control of neural ensemble activity," *Nat. Neurosci.* **21**(6), 881–893 (2018).
12. I.-W. Chen, E. Ronzitti, B. R. Lee, T. L. Daigle, D. Dalkara, H. Zeng, V. Emiliani, and E. Papagiakoumou, "In vivo sub-millisecond two-photon optogenetics with temporally focused patterned light," *J. Neurosci.*

50
51
52
53
54
55
56
57
58
59
60
61
62
63
64
65
66
67
68
69
70
71
72
73
74
75
76
77
78
79
80
81
82
83
84
85
86
87
88
89
90
91
92
93
94
95
96
97
98
99
100
101
102
103
104

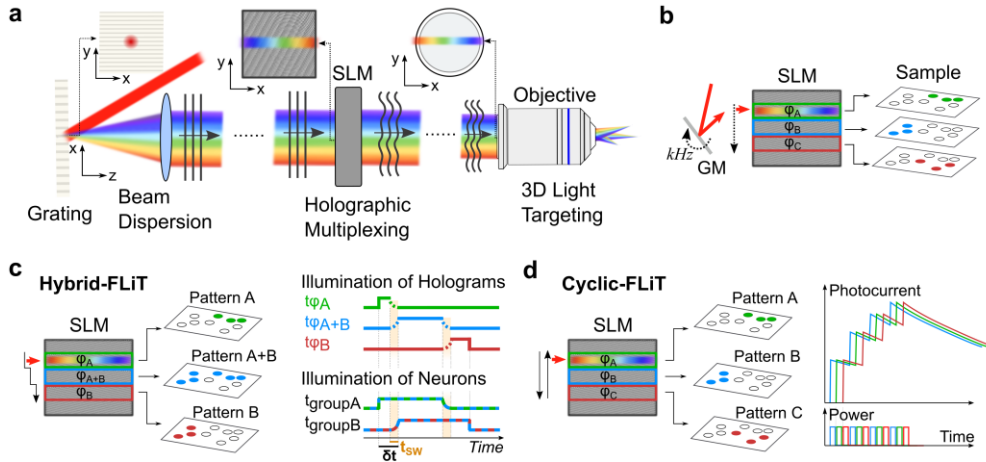
39(18), 1785–18 (2019).

13. G. L. B. Spampinato, E. Ronzitti, V. Zampini, U. Ferrari, F. Trapani, H. Khabou, A. Agraval, D. Dalkara, S. Picaud, E. Papagiakoumou, O. Marre, and V. Emiliani, "All-optical inter-layers functional connectivity investigation in the mouse retina," *Cell Reports Methods* **2**(8), 100268 (2022).
14. J. H. Marshel, Y. S. Kim, T. A. Machado, S. Quirin, B. Benson, J. Kadmon, C. Raja, A. Chibukhchyan, C. Ramakrishnan, M. Inoue, J. C. Shane, D. J. McKnight, S. Yoshizawa, H. E. Kato, S. Ganguli, and K. Deisseroth, "Cortical layer-specific critical dynamics triggering perception," *Science* (80-.). **365**(6453), (2019).
15. L. Carrillo-Reid, S. Han, W. Yang, A. Akrouh, and R. Yuste, "Controlling Visually Guided Behavior by Holographic Recalling of Cortical Ensembles," *Cell* **178**(2), 447-457.e5 (2019).
16. M. dal Maschio, J. C. Donovan, T. O. Helmbrecht, and H. Baier, "Linking Neurons to Network Function and Behavior by Two-Photon Holographic Optogenetics and Volumetric Imaging," *Neuron* **94**(4), 774-789.e5 (2017).
17. J. V. Gill, G. M. Lerman, H. Zhao, B. J. Stetler, D. Rinberg, and S. Shoham, "Precise Holographic Manipulation of Olfactory Circuits Reveals Coding Features Determining Perceptual Detection," *Neuron* **108**(2), 382–393 (2020).
18. C. Lutz, T. T. S. Otis, V. DeSars, S. Charpak, D. a DiGregorio, and V. Emiliani, "Holographic photolysis of caged neurotransmitters.," *Nat. Methods* **5**(9), 821–7 (2008).
19. J. P. Rickgauer and D. W. Tank, "Two-photon excitation of channelrhodopsin-2 at saturation.," *Proc. Natl. Acad. Sci. U. S. A.* **106**(35), 15025–30 (2009).
20. R. Prakash, O. Yizhar, B. Grewe, C. Ramakrishnan, N. Wang, I. Goshen, A. M. Packer, D. S. Peterka, R. Yuste, M. J. Schnitzer, and K. Deisseroth, "Two-photon optogenetic toolbox for fast inhibition, excitation and bistable modulation.," *Nat. Methods* **9**(12), 1171–9 (2012).
21. E. Ronzitti, R. Conti, V. Zampini, D. Tanese, A. J. Foust, N. Klapoetke, E. S. Boyden, E. Papagiakoumou, and V. Emiliani, "Sub-millisecond optogenetic control of neuronal firing with two-photon holographic photoactivation of Chronos," *J. Neurosci.* **37**(44), 10679–10689 (2017).
22. N. Accanto, C. Molinier, D. Tanese, E. Ronzitti, Z. L. Newman, C. Wyart, E. Isacoff, E. Papagiakoumou, and V. Emiliani, "Multiplexed temporally focused light shaping for high-resolution multi-cell targeting," *Optica* **5**(11), 1478 (2018).
23. N. M. Pégard, I. Oldenburg, S. Sridharan, L. Waller, and H. Adesnik, "3D scanless holographic optogenetics with temporal focusing," *Nat. Commun.* 1–14 (2017).
24. B. Sun, P. S. Salter, C. Roider, A. Jesacher, J. Strauss, J. Heberle, M. Schmidt, and M. J. Booth, "Four-dimensional light shaping: manipulating ultrafast spatiotemporal foci in space and time," *Light Sci. Appl.* **7**(1), 17117 (2018).
25. N. C. Pégard, A. R. Mardinly, I. A. Oldenburg, S. Sridharan, L. Waller, and H. Adesnik, "Three-dimensional scanless holographic optogenetics with temporal focusing (3D-SHOT)," *Nat. Commun.* **8**(1), 1228 (2017).
26. D. Oron, E. Tal, and Y. Silberberg, "Scanningless depth-resolved microscopy," *Opt. Express* **13**(5), 1468–1476 (2005).
27. E. Papagiakoumou, V. de Sars, D. Oron, and V. Emiliani, "Patterned two-photon illumination by spatiotemporal shaping of ultrashort pulses," *Opt. Express* **16**(26), 22039 (2008).
28. G. Faini, D. Tanese, C. Molinier, C. Telliez, M. Hamdani, F. Blot, C. Tourain, V. de Sars, F. Del Bene, B. C. Forget, E. Ronzitti, and V. Emiliani, "Ultrafast light targeting for high-throughput precise control of neuronal networks," *Nat. Commun.* **14**(1), 1888 (2023).
29. R. Di Leonardo, F. Ianni, and G. Ruocco, "Computer generation of optimal holograms for optical trap arrays.," *Opt. Express* **15**(4), 1913–22 (2007).
30. O. Hernandez, E. Papagiakoumou, D. Tanese, K. Fidelin, C. Wyart, V. Emiliani, D. Tanese, K. Felin, C. Wyart, and V. Emiliani, "Three-dimensional spatiotemporal focusing of holographic patterns," *Nat. Commun.* **7**, 11928 (2016).
31. S. Choi, P. Kim, R. Boutilier, M. Y. Kim, Y. J. Lee, and H. Lee, "Development of a high speed laser scanning confocal microscope with an acquisition rate up to 200 frames per second," *Opt. Express* **21**(20), 23611 (2013).
32. V. Iyer, T. M. Hoogland, and P. Saggau, "Fast Functional Imaging of Single Neurons Using Random-Access Multiphoton (RAMP) Microscopy," *J. Neurophysiol.* **95**(1), 535–545 (2006).

105 **1. Introduction**

106 The emergence of genetically-encoded light-driven actuators [1–3] has revolutionized
107 neurobiology providing a unique tool to manipulate the activity of neurons with light. In
108 optics, that has spurred the development of several strategies which shape light and activate
109 targeted sets of neurons [4–7], thereby enabling fine-scale control of neural microcircuits [8–
110 12] as mapping connectivity functionally [13] or linking activity patterns to behavior [14–17].

111 Optogenetic light-targeting is generally obtained by shaping the wavefront of a two-
 112 photon (2P) excitation beam, typically with computer-generated phase holograms (CGH)
 113 displayed on liquid-crystal spatial light modulators (LC-SLM) [18]. Few different designs
 114 have been proposed each with its advantages and limitations. The 2P laser can be
 115 holographically split in multiple diffraction-limited spots, which are then spirally scanned on
 116 the targeted cells [8,19,20]. Alternatively, the 2P beam can be patterned in cell-sized spots,
 117 thereby maximizing the number of opsins excited per cell [10] and facilitating precisely timed
 118 spiking events in the neurons [11,12,21]. In this last configuration, a multi-step phase
 119 modulation is typically used [22–24] (Fig.1a). First the beam is tailored in a circular spot
 120 either by using a collimated low-NA gaussian beam [11,25] or providing a light-shaping
 121 phase modulation [12,21]. Second, the spot is projected on a diffracting grating which
 122 disperses the beam and provides for temporal focusing [26], thus axial confinement of the 2P
 123 excitation [26,27]. Finally, the spot is spatially multiplexed by displaying a CGH on a SLM



124 that encodes the 3D coordinates of the targets [22].

125

126 **Fig. 1. Holographic fast-light targeting (FLiT).** (a) Schematics of 3D holographic
 127 multiplexing. A 2P gaussian spot (red beam) is dispersed by a grating in a spatially-chirped
 128 beam and directed to a Spatial Light Modulator (SLM) which multiplexes the gaussian spot on
 129 different x,y,z locations in the sample plane. Top insets indicate the xy beam distribution on
 130 the grating, on the display of the SLM and on the objective back aperture (OBA). (b)
 131 Schematics of FLiT. A galvanometric mirror (GM) switches between holograms tiled on the
 132 SLM, each encoding different light-patterns. (c) Conceptual scheme of *hybrid*-FLiT.
 133 Holograms ϕ_A and ϕ_B on the SLM encode for group of spots A and B, respectively; hologram
 134 ϕ_{A+B} encodes for a pattern including group A and group B. By switching the beam vertically
 135 across the three holograms with predetermined dwell-times (t_{ϕ_A} , t_{ϕ_B} , $t_{\phi_{A+B}}$) and illumination
 136 powers (P_{ϕ_A} , P_{ϕ_B} , $P_{\phi_{A+B}} = P_{\phi_A} + P_{\phi_B}$) per each mask, it is possible to set an arbitrary δt delay ($\delta t =$
 137 $t_{\phi_A} + t_{SW}$) of activation between the two groups of spots which are illuminated for total durations
 138 $t_{groupA} = t_{\phi_A} + t_{\phi_{A+B}}$ and $t_{groupB} = t_{\phi_B} + t_{\phi_{A+B}}$. t_{SW} indicates the switching time to reposition the laser
 139 beam from one hologram to the next. (d) Conceptual scheme of *cyclic*-FLiT. Different
 140 holograms on the SLM encode for different multi-cell patterns. The illumination beam is
 141 cyclically scanned across the holograms and a cyclic photoactivation process is enabled on the
 142 different light patterns in parallel.

143

144 It is critical to note that, for low-NA gaussian beams (and also for generalized phase
145 contrast beams) [10,24], the beam diffracted by the grating results in a line focus beam of
146 dispersed colors on the SLM, which underfills the multiplexing SLM display in the direction
147 orthogonal to the dispersion (Fig.1a, insets). Taking advantage of this line focused
148 illumination, we recently proposed an optical system for fast light-targeting (FLiT) where the
149 SLM is parallelly addressed with H distinct tiled holograms and an upstream galvanometric
150 mirror is used to rapidly switch the line focus beam among them (Fig.1b) [28]. This enabled
151 to demonstrate two new illumination protocols for optogenetic multi target stimulations. A
152 first one, that we termed hybrid-FLiT (Fig.1c), enables tuning the relative firing time of $\frac{H+1}{2}$
153 groups of cells with μs -range temporal precision. The second one, that we termed, cyclic-
154 FLiT (Fig.1d), enables multi target stimulation using \sqrt{H} to H -times less power than what
155 used in conventional holography and so to proportionally scale up the number of achievable
156 targets and/or reduce sample heating.

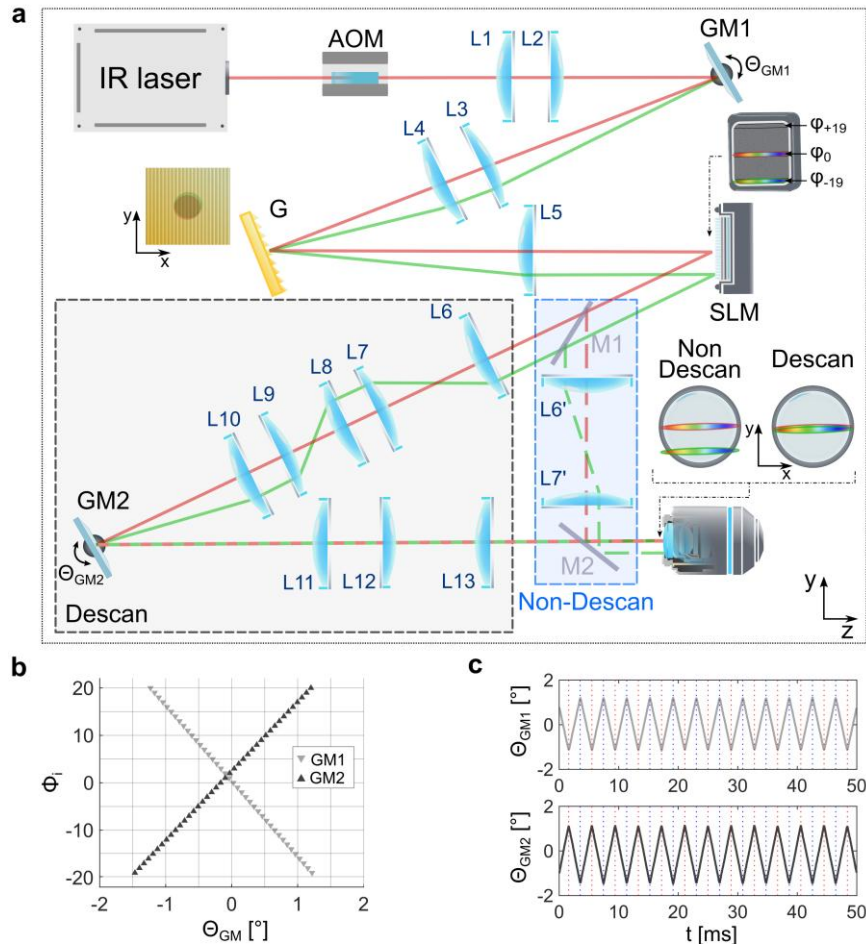
157 In both configurations, the tilt and drop of power induced by the objective back aperture
158 to the off-axis holograms (i.e. situated at the edges of the SLM and at the side of the objective
159 back aperture), have limited the usable holograms to those close to the pupil center,
160 corresponding to $\sim 50\%$ of the total SLM vertical size and have generated tilting in the
161 volumes of excitation. To overcome these limitations, we here propose an alternative scheme
162 incorporating a de-scan unit which allows rapidly switching among different holograms while
163 steadily maintaining the illumination beam in the middle of the illumination objective pupil.
164 We demonstrated that this configuration enables to use the entire SLM vertical size and reach
165 uniform on-axis volumes of excitation.

166 2. Materials and Methods

167 2.1 Optical system

168 The optical system (Fig. 2a) comprised two optical paths for descanned FLiT (deFLiT,
169 Fig 2a, grey area), and conventional FLiT (Fig.2a, blue area) configuration. The system was
170 supplied by a Ti:Sapphire laser tuned at 920nm (Chameleon Ultra II, Coherent, repetition rate
171 80MHz, pulse width 100 fs, 1.5W max output power). Power was controlled by an acousto-
172 optic modulator (AOM) for fast intensity modulation (AA Opto-Electronic, France). The
173 laser beam was initially demagnified with a 4f telescope ($f_1=500\text{mm}$, $f_2=300\text{mm}$) and
174 collimated onto a pair of galvanometric mirrors (GM1) (3 mm aperture, protected silver
175 coating, 6215H series; Cambridge Technology). GM1 plane was conjugated by means of a
176 magnifying telescope ($f_3=200\text{mm}$, $f_4=400\text{mm}$) to a reflective dispersion grating of 800
177 lines/mm used to temporally focus [26,27] the pulse of the beam. The spatially-chirped beam
178 diffracted by the grating was focused by a lens ($f_5=500\text{mm}$) on a reconfigurable liquid-
179 crystal-silicon spatial light modulator LC-SLM (LCOS-SLM X10468-07, Hamamatsu
180 Photonics, resolution 800×600 pixels, $20\mu\text{m}$ pixel size), located in the Fourier plane of the
181 diffraction grating. In the deFLiT path (Fig.2a, grey area: descanned path), the beam reflected
182 by the SLM was Fourier Transformed by a lens ($f_6=300\text{mm}$) and then relayed ($f_7=500\text{mm}$,
183 $f_8=250\text{mm}$; $f_9=400\text{mm}$, $f_{10}=150\text{mm}$) onto a second pair of galvanometric mirrors (GM2) (3
184 mm aperture, protected silver coating, 6215H series; Cambridge Technology). The beam
185 reflected by GM2 was inversely Fourier transformed ($f_{11}=100\text{mm}$) and imaged at the
186 objective back aperture (OBA) of a microscope objective (Olympus LUMPlanFL 40XW NA
187 0.8) through a final telescope ($f_{12}=1000\text{mm}$, $f_{13}=500\text{mm}$) to match the size of the objective
188 back aperture. In the non-descanned path (Fig.2a, blue area), the LC-SLM was directly
189 conjugated to the OBA with a single telescope ($f_{14}=750\text{mm}$, $f_{15}=750\text{mm}$). Two removable
190 mirrors (M1, M2) allowed switching between the two paths. Lenses between the LC-SLM

191 and the OBA in both FLiT and deFLiT paths were chosen as to fill the OBA with the chirped
 192 illumination in order to maximize the effect of temporal focusing on the axial resolution. The
 193 total de-magnification of the LC-SLM size at the OBA for FLiT and deFLiT was ~ 1 and
 194 ~ 0.9 , respectively.
 195



196 **Fig. 2. Descanned holographic fast-light targeting (deFLiT)** (a) Scheme of the
 197 experimental setup of deFLiT. Red and green beams represent the light pathway of a beam
 198 illuminating holograms on the edges (green) or in the middle (red) of the SLM. Blue and gray
 199 outlines show the non-descanned and the descanned pathway, respectively. Insets indicate xy
 200 beam distribution on the SLM (green and red beams are spatially shifted), on the grating and
 201 on the OBA (green/red beams overlapping in descanned and are separated in non-descanned
 202 mode). AOM: Acousto-Optic Modulator; L: Lens; M: movable Mirror; GM: Galvanometric
 203 Mirror; SLM: Spatial Light Modulator; G: Grating. (b) Tilting angle of the galvanometric
 204 mirrors GM1 and GM2 depending on the tiled hologram addressed on the SLM. SLM was
 205 subdivided in 39 equal tiled horizontal holograms. (c) Synchronized time courses of the tilting
 206 angle for GM1 and GM2 when scanning the full SLM extent in a cyclic manner.

207
 208 Following a previously validated computation scheme [28], the LC-SLM was addressed
 209 with multiple independent holograms, vertically aligned along the y-direction (i.e the
 210 direction perpendicular to the grating's dispersion). In particular, the SLM was subdivided in

211 up to 39 holograms ϕ_i , with $i=0$ and $i=\pm 19$ corresponding to the hologram located in the
212 middle and at the edges of the SLM display, respectively (1 hologram = 600x20 pixels)
213 (Fig.2a, inset). Each hologram was encoded to generate arbitrary 2D or 3D patterns of
214 gaussian spots in the sample plane by using a weighted Gerchberg and Saxton algorithm [29].
215 The zero order was physically blocked in the image plane of the lens after the SLM. After
216 dispersion through the grating for temporal focusing, the spatially-chirped beam was scanned
217 through the multiple holograms by controlling the tilting angle of GM1 (Fig.2b, light grey).
218 For the deFLiT configuration, the second galvo GM2 was synchronized and driven with
219 counter-phasing signals with respect to GM1 (Fig.2b dark grey,c), which allowed descanning
220 the beam and maintaining a stationary non-tilted illumination at the center of the objective
221 back aperture. Each GM unit was driven by a servo driver (MicroMax series 671; Cambridge
222 Technology) controlled by a digital/analog converter board (PCI-6110; National Instrument).
223 XYZ offsets of holographic spots coordinates caused by different off-axis holograms were
224 calibrated and compensated. The control of the system was fully automatized through a
225 homemade software written in Python 3 and using the open graphic library PyQt5 which
226 allowed automatic calculation of the tiled holograms and synchronized control of the GM
227 rotation and AOM attenuation. To measure the illumination at the OBA for deFLiT and FLiT,
228 a CMOS camera (Thorlabs, DCC1545M) was placed at the OBA while controlling the
229 position of GM1 to switch among the two paths. The light intensity distribution used to
230 illuminate the holograms was characterized in terms of horizontal and lateral widths, obtained
231 from the gaussian fit of the vertical and horizontal cross sections using ImageJ.

232 *2.2 Optical Characterization of Two-Photon Excitation*

233 In order to optically characterize the spatial resolution and the intensity distribution of the
234 holographic spots, 2PE fluorescence from a thin ($\sim 1 \mu\text{m}$) spin-coated layer of rhodamine-6G
235 in polymethyl methacrylate 2% w/v in chloroform was induced by projection of holographic
236 illumination patterns through the excitation objective (Olympus LUMPlanFL 40XW NA 0.8)
237 and was collected through an opposite imaging objective (Olympus LUMPlanFL 60XW NA
238 0.9) in a transmission geometry on a sCMOS camera (pco, panda 4.2 bi). A short-pass filter
239 was used to reject the laser light (Semrock, Brightline Multiphoton Filter 680/sp). 3D stacks
240 were collected by maintaining the imaging objective in a fixed position and axially moving
241 the excitation objective with $1 \mu\text{m}$ steps by means of a piezoelectric motor along the z-
242 direction. The axial distribution of intensity on different spots was measured by integrating
243 the pixel intensity across circular region of observations (ROIs) around the spots in each z
244 plane. The intensity and axial resolution for each spot have been evaluated and reported as
245 maximum intensity and Full Width Half Maximum (FWHM), respectively. Images have been
246 analyzed with ImageJ and 3D rendering is performed with Imaris. To measure the tilt of the
247 volumes of excitation enabled by different holograms Φ_i , we computed for each hologram 2
248 axially-separated spots at the nominal coordinates $(x,y,z) = (0,0,\pm 50) \mu\text{m}$. We then acquired
249 the corresponding 3D stacks and we measured the angle θ_i between the objective optical axis
250 and the line joining the center of the 2 spots.

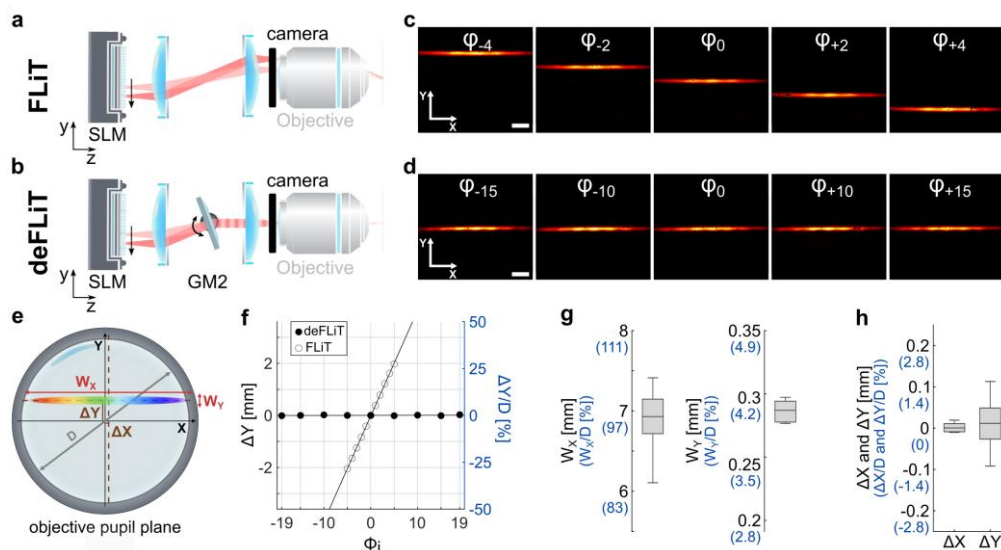
251 *2.3 Modeling of the Impact of Beam Diaphragming on 2P Excitation Efficiency*

252 The signal generated by a 2P excitation process can be expressed as $S_{2P} = \gamma P^2 / f \tau$, where
253 P is the averaged illumination power, τ is the laser pulse width, f is the laser repetition rate
254 and γ is a multiplicative constant including the cross-section and the quantum yield of the

255 excited molecule. To model how the generated S_{2P} signal was affected by beam
 256 diaphragming at the objective pupil plane for deFLiT illumination, we modeled the
 257 illumination shape at the OBA for each hologram with an elliptic gaussian light distribution
 258 of width W_x and W_y at position (x_i, y_i) in the x and y directions, respectively. Estimations for
 259 W_x and W_y , and (x_i, y_i) positions were directly obtained by fitting the X- and Y- experimental
 260 intensity profiles of the beams taken at the OBA with a CMOS camera with gaussian curves .
 261 The fraction of transmitted average power $P(\phi_i)$ for each hologram position, was then
 262 estimated by considering the geometrical intersection between the elliptic beams
 263 corresponding to each hologram and the OBA. To estimate how the OBA affected the pulse
 264 durations $\tau(\Phi_i)$, we simulated for each hologram position the spatial chirp of the beam at the
 265 OBA using the spectral bandwidth of the laser ($\Delta\lambda=12.5\text{nm}$), the grating frequency and the
 266 optical path, and weighting the effect of the pupil cross-section on each spectral component.
 267 We then obtained the transmitted temporal pulse width $\tau(\Phi_i)$ at the sample through the
 268 Fourier transform of the resulting bandwidth. The resulting 2P signal produced by each
 269 hologram is then calculated using the expression: $S_{2P}(\Phi_i) = \gamma P(\Phi_i)^2 / f \tau(\Phi_i)$. In particular,
 270 we considered two different OBA illuminations either given by an SLM-to-OBA
 271 magnification equal to 1 (as in the current FLiT setup) or 0.9 (as in the current deFLiT setup).
 272 This last case allowed a more accurate comparison of the expected performances of FLiT and
 273 deFLiT in the very same OBA illumination conditions.

274 3. Results

275 To compare the descanned configuration, deFLiT, with the previously presented FLiT
 276 configuration we first used a CMOS camera at the objective back aperture (OBA) plane to
 277 monitor the spatial distribution of the incoming beam plane while scanning the chirped
 278 excitation beam between the different holograms (Fig. 3) following the *descan* and the *scan*
 279 paths (Fig. 2a, grey and blue areas).
 280



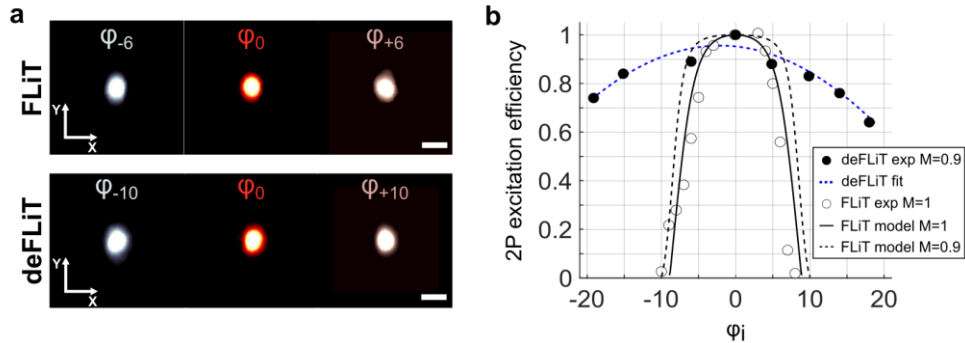
281 **Fig. 3. Light distribution at the objective entrance with descanned-FLiT.** (a,b)
 282 Schematics of the detection scheme to image the incoming beam with a CMOS camera at the
 283 OBA for non-descanned FLiT (a) and descanned FLiT (b). (c,d) XY intensity distribution of

284
285
286
287
288
289
290
291
292
293
294
295
296

the beam at the OBA for different tiled holograms in FLiT (c) and deFLiT (d). The SLM was subdivided in 39 horizontal rectangular holograms ϕ_i (with $i=0$ and $i=\pm 19$ the holograms in the middle and at the edges of the SLM, respectively). Scale bar 1mm. (e) Schematics of a temporally-focused line beam at the OBA plane. W_x , W_y and ΔX , ΔY represent the beam-waists and the beam-shifts in the x- and y-directions, respectively. y-direction orthogonal to the grating dispersion. D is the OBA diameter. (f) ΔY displacement of the beam for FLiT (empty circles) and deFLiT (filled circles) in mm (left, black y-axis) and as a percentage of the pupil diameter D (right, blue y-axis). Fittings are indicated with black lines. (g,h) Variation of the beam-waists W_x and W_y (g) and beam-shifts ΔX and ΔY (h) along the x- and y-directions at the OBA for different holograms in deFLiT, extracted from Gaussian fittings of the illumination profiles in (d). W_x , W_y , ΔX and ΔY distributions are reported in mm (black y-axes) and as a percentage of the pupil diameter D (blue y-axes). Bars and middle horizontal lines indicate standard deviations and means.

297
298
299
300
301
302
303
304
305
306
307
308
309
310
311
312

We subdivided the SLM in 39 tiled holograms ϕ_i (Fig.2a, inset), vertically aligned in the direction orthogonal to the grating dispersion (y-direction). We used the galvanometric mirror GM1 to scan the spatially chirped beam onto the SLM between the different holograms (Fig1b). In the FLiT configuration, the OBA and LC-SLM planes are directly conjugated (Fig.3a) and the ellipsoidal chirped beam which scans the different holograms of the LC-SLM also vertically scans the OBA (Fig. 3c,e,f). Opposite to that, in deFLiT, a second galvo unit GM2 counteracts the beam scanning from GM1 (Fig.3b) maintaining the illumination beam in the middle of the OBA (Fig.3d,f). Importantly, we observed that during the descan process, the spatial distribution of the beams at the OBA was substantially unaltered, with an averaged beam waist among the different holograms of $0.29 \pm 0.03 \text{mm}$ and $6.9 \pm 0.4 \text{mm}$ (as mean \pm st.dev., respectively in the x- and y- directions) (Fig.3g). Also, spatial oscillations of the beam during descan were negligible, corresponding to spatial fluctuations around the OBA center as low as $\pm 12 \mu\text{m}$ and $\pm 91 \mu\text{m}$ in the x- and y-directions, equal to $\pm 0.2\%$ and $\pm 1.3\%$ of the pupil diameter (Fig.3h).

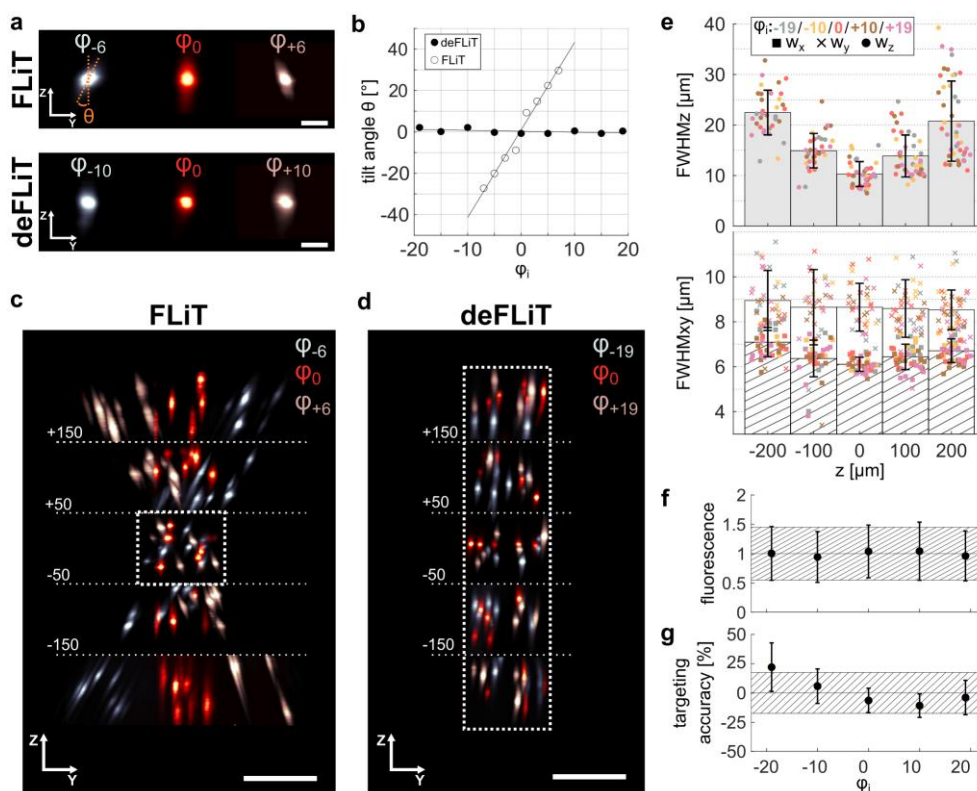


313
314
315
316
317
318
319
320
321

Fig. 4. In-focus holographic light-patterns. (a) Representative XY images of the 2P fluorescence induced by a single spot encoded by different tiled holograms (according to the hologram number indicated in the figure) for FLiT and deFLiT. Scale bar $10 \mu\text{m}$. (b) Variation of the experimental 2P excitation intensity of a single spot encoded by different tiled holograms for FLiT (empty circles) and deFLiT (filled circles). Blue dashed line is a polynomial fit of the deFLiT experimental data. Black solid line indicates the expected variation given by the experimental beam geometry (details in methods) for the FLiT system. Black dashed line indicates the expected variation in a FLiT system by assuming equal SLM-to-OBA magnification for FLiT and deFLiT.

322
 323
 324
 325
 326
 327
 328
 329
 330
 331
 332
 333
 334
 335
 336
 337
 338
 339
 340
 341

Next, we analyzed the intensity distribution generated onto the sample by the different holograms in the two configurations as a function of the hologram position on the SLM. For this, we encoded each of the 39 tiled holograms to generate a single spot at the objective focal plane and measured the corresponding 2PE-fluorescence onto a thin layer of Rhodamine 6G. We observed that the xy shape of the holographic spots was substantially unaltered in both cases (Fig.4a). However, as expected, in the case of FLiT, the fluorescence intensity decreased as the position of the corresponding hologram imaged at the OBA moved away from the center, reaching nearly 50% of the 2P fluorescence intensity produced by the central hologram ϕ_0 , for the holograms ϕ_{-6} and ϕ_{+6} (corresponding to beam shifts of ± 2.4 mm at the OBA, equivalent to $\pm 33\%$ of the OBA diameter), and dropping to zero ($< 3\%$ of relative 2P fluorescence intensity) for holograms ϕ_{-10} and ϕ_{+8} (corresponding to beam shifts of -4.1 mm and $+3.2$ mm at the OBA, equivalent to -57% and 45% of the OBA diameter, respectively) (Fig.4b). These results are in agreement with theoretical simulations of 2P intensity drops due to pupil diaphragming (Fig 4b, plain and dashed black curves and methods for modeling details). Conversely, the experimental deFLiT system enabled maintaining $> 75\%$ of the 2P signal up to the ϕ_{-19} and ϕ_{+12} holograms (Fig.4b, black dots). Residual power losses for the most distal holograms were likely due to distortions or partial crops of the beam when travelling at very off-axis edges of the optics between GM1 and GM2.



342
 343
 344
 345
 346
 347

Fig. 5. Volumetric distribution of multi-spots holographic light-patterns. (a) YZ intensity projection of spots generated in the center of the field of excitation by different tiled holograms (according to the hologram number indicated in the figure) for FLiT and deFLiT, respectively. Scale bar $10\mu\text{m}$. (b) Angle θ between the optical axis and the tilted axial axis of the holographic spot in the center of the FOE as in (a) for different tiled holograms, in FLiT (empty circles) and deFLiT (filled circles). (c-d) YZ intensity distributions of 3D randomly

348 distributed spots generated by different tiled holograms for FLiT (c) and deFLiT (d) over an
349 axial range of 500 μm . Scale bar 100 μm . Different colors correspond to different tiled
350 holograms. (e) Axial (top) and lateral (bottom) FWHMs of the intensity profiles of spots
351 randomly generated in 3D, for deFLiT as in (d), against their axial position. Each marker
352 represents one spot. Different colors indicate spots encoded by different tiled holograms. Bars
353 indicate the mean values in 100 μm range around the designated z position. Vertical lines
354 indicate st. dev. (n=194 spots). (f) 2PE fluorescence of 3D random spots in deFLiT mode as in
355 (d) obtained with different holograms. The dots and the error bars represent the mean and std
356 per hologram, respectively. The black horizontal line and dashed area represent the global
357 mean and std. (n=194 spots). (g) Spot targeting accuracy when targeting n=45 spot locations,
358 randomly distributed across a 120x120x500 μm^3 in deFLiT mode, with different tiled
359 holograms. For each spot location, spot targeting accuracy of hologram φ_i is defined as the
360 distance between the experimentally reached position using hologram φ_i and the barycenter of
361 the positions reached with holograms φ_{-10} , φ_{-10} , φ_0 , φ_{+10} and φ_{+20} for this spot, divided by the
362 mean spot size. Dots and error bars represent the mean and std per hologram, respectively. The
363 black horizontal lines and dashed area represent the global mean and std. (n=45 per hologram
364 φ_i).

365
366 We then characterized, for the two cases, the capability to generate 3D patterns of spots. As
367 previously reported [28], in FLiT, off-axis holograms at the OBA obliquely illuminated the
368 sample which resulted in axially tilted spots and volumes of excitations (Fig.5a). For
369 holograms from φ_{-6} to φ_{+6} , we measured an axial tilt from -24° to $+26^\circ$ (Fig.5b). This
370 restricted the portion of excitation volume where the different holograms could overlap to a
371 region of 120 x 120 x 100 μm^3 (Fig. 5c, white dashed rectangle). Opposite to that, for
372 deFLiT, the scan of the 39 holograms at the SLM plane gave rise to a negligible optical axis
373 tilt ($0.3\pm 1.1^\circ$, as mean \pm st.dev. spot axial tilt) (Fig.5a, b). Consequently, deFLiT provided
374 on-axis colocalized excitation over 120 x 120 x 500 μm^3 (Fig.5d). Within this volume, we
375 measured an axial resolution of $10 \pm 2 \mu\text{m}$ in the perifocal region (assumed $\pm 50 \mu\text{m}$ from
376 focal plane) and of up to $22\pm 7 \mu\text{m}$ in the distal portion of the volume (Fig.5e), and the axial
377 resolution was homogeneous among all holograms. The lateral spot sizes were $6.5\pm 0.7\mu\text{m}$
378 and $8.7\pm 1.3\mu\text{m}$ along the x- and y-direction, respectively, and were homogenous along the z-
379 axis and among holograms (Fig.5e). Consistently with previous findings for conventional
380 holography [22], fluorescence variation within the excitation volume from different spots was
381 below 45% (st.dev), and was homogenous across different holograms (Fig.5f). We finally
382 assessed the deFLiT light-targeting accuracy (here defined as the difference between the set
383 and actual spot position) among holograms generated within this volume by encoding the
384 same 3D patterns to different tiled holograms. We obtained an average targeting accuracy
385 below 18% of the spot extension (Fig.5g), which indicates that minor excitation variabilities
386 are expected when sweeping between holograms.

387 4. Discussion

388 We have developed and characterized a descanned variant, named deFLiT, of a previously
389 reported optical scheme for ultra-fast sequential light targeting (FLiT) based on the rapid
390 switching of a temporally focused beam between H vertically aligned holograms on a SLM at
391 kHz rates. We demonstrated that FLiT enables an ultra-fast sequential stimulation of $(H+1)/2$
392 distinct targets and, using cyclic illumination, multi-target optogenetic activation with \sqrt{H} - to
393 H - times reduced power with respect to conventional holography [28].

394 In the original FLiT configuration, a relay telescope is used to directly image the SLM
395 display onto the OBA. Off-centered holograms tiled on the SLM are thus relayed off-axis at

396 the OBA, which then leads to axial tilts of the holographic illumination onto the sample.
397 Also, off-centered holograms are partly cropped at the sides, which leads to a proportional
398 intensity cut of the corresponding generated patterns. Minimizing these effects requires
399 maximizing the number of holograms projected into the middle region of the objective pupil.
400 This can be achieved by reducing the magnification between the SLM and the OBA and so by
401 underfilling the OBA. This however also reduces the effective objective NA, and therefore
402 enlarges the axial resolution. Alternatively, each hologram on the SLM can be narrowed by
403 reducing the number of pixels per hologram in the y-direction so to increase the hologram
404 number in the central OBA region. This however also reduces the amount of encodable
405 information per hologram [30] and limits the maximum deliverable power per hologram
406 (limited by the SLM damage threshold). For example, in a previously demonstrated
407 configuration for FLiT, a trade-off between axial resolution, excitation volume (FOE),
408 number of illuminated holograms (H), and power losses below 33% was reached [28] by
409 using a small pixel pitch ($12.5\mu\text{m}$) SLM tiled in 45 holograms, a large aperture objective (20x
410 magnification, 1.0 NA) and the 23 central holograms (corresponding to 51% of the total SLM
411 vertical size).

412 In the present manuscript, we propose an alternative optical design, deFLiT, where a second
413 scanning unit enables to project the illuminated hologram always at the center of the OBA
414 independently of the position of the illuminated hologram on the SLM. We demonstrate that
415 by using a conventional large pixel size-SLM ($20\mu\text{m}$) and a 40x, 0.8 NA objective we could
416 use 100% of the SLM (divided in 39 holograms) with power losses below 18%, and an on-
417 axis colocalized excitation volume, FOE, of $120\times 120\times 500\mu\text{m}^3$. For comparison, maintaining
418 the power losses below 18% with a non-descanned-FLiT system using the same SLM divided
419 in 39 holograms, same objective and same SLM-to-objective magnification, would limit to
420 use only the 12 most central holograms (i.e. only 31% of the SLM vertical size) and would
421 reach tilted excitation volumes.

422 While deFLiT refines the performances of FLiT for any SLM/objective system, deFLiT
423 presents the disadvantage of a more complex optical system and thus also a more complex
424 alignment. In particular, the holographic pattern generated in the Fourier plane after the SLM
425 must be de-magnified to fit on the descanned mirrors. In the present design, 3mm-size descanned
426 mirrors are used for maximal speed, therefore a 4-lenses telescope is needed to fit the
427 holographic FOE on them, which introduces power losses and aberrations for beams
428 travelling at very off-axis edges of the optics between GM1 and GM2. These undesirable
429 effects could be mitigated by using larger galvanometric mirrors although in this case longer
430 response times are expected. Alternative designs featuring different scan units could also be
431 considered. These include polygonal scanning mirrors [31], acousto-optic deflectors [32] or
432 rotating phase masks - that could encode prism-like phase modulation to tilt the beam in a
433 transmission geometry.

434 In conclusion, we demonstrated deFLiT as an alternative design to FLiT, enabling to
435 maximize the performances of FLiT in terms of number of usable holograms and reachable
436 excitation volume. This configuration is especially indicated for configurations using high-
437 magnification objectives and/or conventional large pixel ($20\mu\text{m}$) SLMs.

439 **Funding.** This work was supported by the ERC (HOLOVIS; ERC2019-ADG-
440 885090), ERC Horizon 2020 H2020-ICT (DEEPER, 101016787), the IHU - FOReSIGHT

441 (Grant P-ALLOP3-IHU-000), the Région Île-de-France (Grant WASCO, DIM-Elicit) the
442 NIH Brain initiative (Grant 1RF1NS128772-01).

443 **Acknowledgments.** We thank Clément Molinier for the development of the software for
444 phase masks generation and SLM control and Christophe Tourain for technical support on the
445 electronics.

446 **Disclosures.** The authors declare that there are no conflicts of interest related to this
447 article.

448 **Data availability.** Data underlying the results presented in this paper are not publicly
449 available at this time but may be obtained from the authors upon reasonable request.

450 **Supplemental document.** N/A.

451